Electronic Supplementary Material (ESI) for ChemComm.

Supporting Information

Surface configuration of CO adsorbed on nanostructured Pt electrodes probed with broadband sum frequency generation spectroscopy

Zhi-Chao Huang-Fu, Qian-Tong Song, Yu-Han He, Xiao-Lin Liu, Jing-Jing Wang, Shi-Gang Sun and Zhao-Hui Wang**

Collaborative Innovation Center of Chemistry for Energy Materials, State Key Laboratory for Physical Chemistry of Solid Surface, Department of Chemistry, College of Chemistry and Chemical Engineering, Xiamen University, Xiamen 361005, China. E-mail: sgsun@xmu.edu.cn, zhwang@xmu.edu.cn.

Experimental Procedures

1. Preparation of Pt nanostructured electrodes and electrochemical measurements

The Pt thin layers were deposited electrochemically on GC electrodes by cyclic voltammetric (CV) treatment in the solution of 2 mM K_2PtCl_6 (in 0.5 M H_2SO_4). An EG&G 263A potentiostat/galvanostat was employed to control the surface potential. A saturated calomel electrode (SCE) was employed as the reference electrode, a flame-annealed Pt foil (99.99%) as the counter electrode. The GC electrodes were mechanically polished by successively using 5, 1, 0.3 μm alumina powders. The surface potential was cycling between -0.24 V to 0.4 V and the sweep rate was 50 mV/s. A series of nm-Pt electrodes with different NPs coverages on GC were prepared by varying the number *n* of potential cycles, and was denoted as nm-Pt/GC*(n)*. All solutions were prepared with Millipore-Q ultra-pure water (18.2MΩ·cm) and were de-aerated by bubbling high-pure N_2 gas (99.99%, Linde) for 15 min before CV measurements.

CO adsorption onto Pt surface was realized by bubbling CO gas (>99.9%, Linde) into the cell at 0 mV surface potential. Then, N_2 gas was bubbling for more than 30 min to remove CO in the solution, and maintain O_2-free for the subsequent spectroscopic measurements.

2. BB-SFG measurements

The BB-SFG spectroelectrochemistry apparatus was described elsewhere.[1-4] Briefly, the output of a femtosecond Ti:Sapphire laser (Coherent Inc., Legend Elite Duo) was used to pump two optical parametric amplifiers (Light Conversion) to generate tunable broadband infrared pulses (IR, 150 fs, 160 cm^{-1} FWHM) and narrowband visible pulses (VIS, 2.5 ps, 7 cm^{-1} FWHM). For CO_{ad}, the 760 nm VIS (1 μJ/pulse) and 4800 nm IR (9 μJ/pulse) were overlapped on the electrode surface with approximately 60° incident angles. All the BB-SFG spectra were acquired under the *ppp* polarization combination (*p*-SFG, *p*-VIS, *p*-IR), and recorded by a spectrograph (Andor Technology, SR-303i-B) with a CCD detector (Andor Technology, DU920P-BR-DD).

In situ BB-SFG experiments were carried out in a home-made electrochemical cell.[3, 5] The working electrode was a bulk polycrystalline Pt (bulk-Pt for short) or a GC cylinder (6 mm, a geometric area of 0.28 cm^2) with nm-Pt films, which was embedded in the PTFE holders. A Pt foil and the SCE electrode served as the counter and reference electrodes, respectively. The surface potential was controlled by a CHI604D potentiostat during the SFG measurements.

Details of the SFG principle have been discussed elsewhere.[6-11]

In BB-SFG, a picosecond visible light ω_{VIS} (VIS) and a femtosecond infrared light ω_{IR} (IR) are used to generate the SFG signal at $\omega_{SFG} = \omega_{VIS} + \omega_{IR}$. The intensity of the SFG signal, $I_{SFG}(\omega)$, is given by,

$$I_{\mathrm{SFG}} \propto |P_{\mathrm{SFG}}(\omega)|^2 = |\chi^{(2)} E_{\mathrm{IR}} E_{\mathrm{VIS}}|^2 \qquad \text{Equation S1}$$

where P_{SFG} is the induced polarization, and $\chi^{(2)}$ is the second order susceptibility. $\chi^{(2)}$ can be separated into contributions of the infrared-frequency dependent resonances of the adsorbates, $\chi^{(2)}_{\mathrm{R}}$, and nonresonant (NR) contribution of the interfacial electrons, $\chi^{(2)}_{\mathrm{NR}}$, which is insensitive to the IR frequency (mainly from the electrode surfaces herein) and expressed as Equation S2,

$$\chi^{(2)} = \chi^{(2)}_{\mathrm{NR}} + \chi^{(2)}_{\mathrm{R}} = \chi^{(2)}_{\mathrm{NR}} + \sum_q \frac{A_q e^{i\theta_q}}{(\omega_{\mathrm{IR}} - \omega_q)i + \Gamma_q} \qquad \text{Equation S2}$$

where A_{q}, θ_{q}, ω_{q} and Γ_{q} are the resonant oscillation amplitude, relative phase, frequency and half width at half maximum of the q^{th} mode vibrations of the resonances, respectively.

3. Electrochemical in Situ FTIR Spectroscopy

Electrochemical *in situ* FTIR spectroscopy (*in situ* FTIRS) experiments were performed on a Nicolet 8700 Infrared spectrometer (Nicolet) equipped with a liquid nitrogen cooled MCT-A detector in the external reflection configuration. Details of the *in situ* FTIRS studies have been reported elsewhere.[12, 13] The results are presented in the form of relative change in reflectivity, i.e.

$$\frac{\Delta R}{R} = \frac{R(E_S) - R(E_R)}{R(E_R)} \qquad \text{Equation S3}$$

where $R(E_{\mathrm{S}})$ and $R(E_{\mathrm{R}})$ are the single-beam spectra of the reflection collected at sample potential E_{S} and reference potential E_{R}, respectively. In this paper, the reference potential was fixed at 0.80 V at which the $\mathrm{CO_{ad}}$ could be oxidized immediately and completely to $\mathrm{CO_2}$. Spectral resolution in this study was 8 $\mathrm{cm^{-1}}$ and each spectrum was coadded 400 interferograms (84 s).

Results and Discussion

1. Characterizations of the nm-Pt/GC electrodes

Figure S1 shows the scanning electron micrographs (SEM) of the nm-Pt electrodes. These nm-Pt/GC(*n*) electrodes consist of Pt NPs deposited on glassy carbon surfaces with a mean diameter around 80 nm. The average size of the Pt NPs slightly increases from 74.8 nm to 86.6 nm with the increase of the cycling number *n*, the shape of the Pt NPs remains as irregular nano polyhedrons. However, more significant change is the aggregation of the Pt NPs, the coverage of the Pt NPs on GC grew progressively as *n* increased. With the aggregation of Pt NPs, the electrode surface transitions from island structure to lumpish structure. Figure S2 shows the cyclic voltammograms (CVs) of these nm-Pt/GC electrodes and the bulk-Pt electrode in 0.1 M H_2SO_4 between -0.24 and 0.75 V. The broad bands around -0.24 to 0.10 V are the adsorption and desorption of hydrogen on Pt. By integrating the charge of this band for each electrode, the surface sites for hydrogen adsorption can be calculated, and then the electrochemically active surface area (ECSA) of the Pt surfaces could be estimated (use the electric charge density value of 210 $\mu C \cdot cm^{-2}$ from a perfect polycrystalline Pt electrode as reference). The results are shown in Table S1.

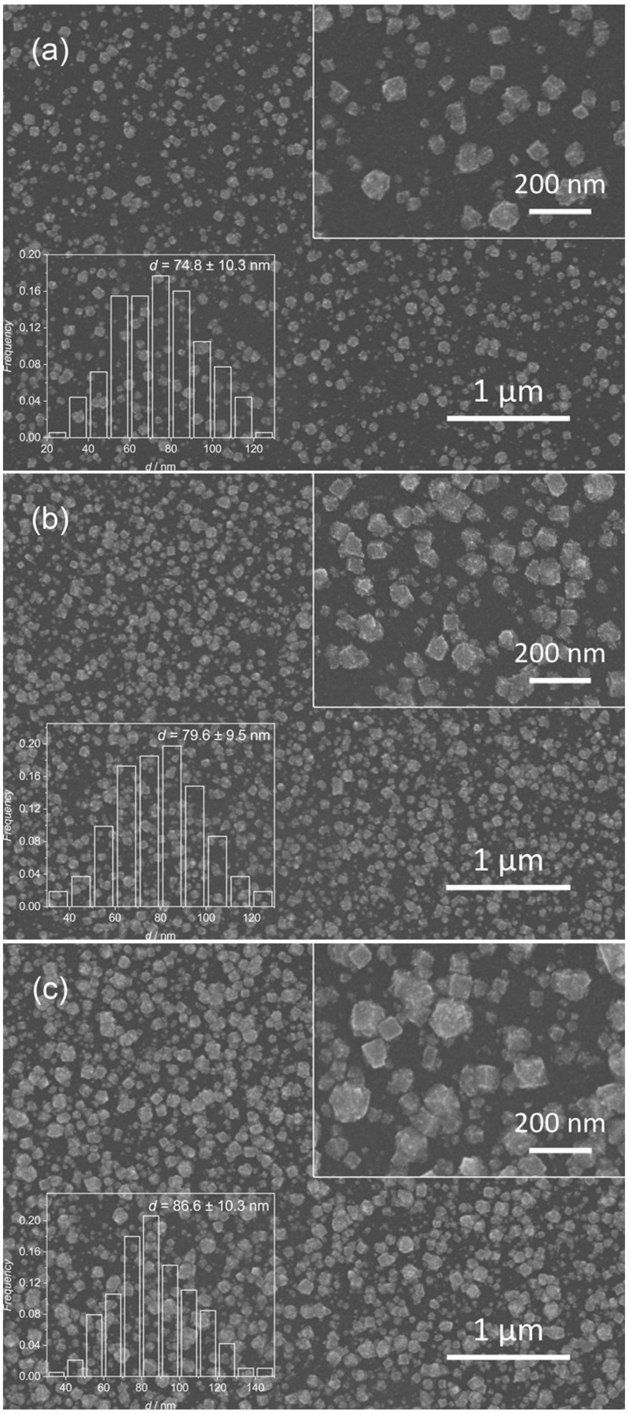

Figure S1. SEM images of the nm-Pt deposited on glassy carbon electrodes and size distribution of the NPs. (a) nm-Pt/GC(5), (b) nm-Pt/GC(10), (c) nm-Pt/GC(15).

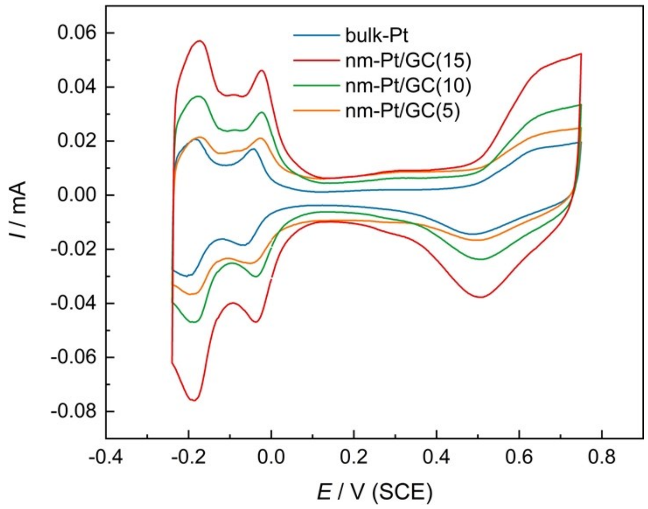

Figure S2. CVs for nm-Pt/GC(*n*) electrodes and the bulk-Pt electrode in 0.1M H_2SO_4 solution.

Table S1. Electrochemically active surface area of the Pt electrodes.

	bulk-Pt	nm-Pt/GC(5)	nm-Pt/GC(10)	nm-Pt/GC(15)
ECSA (cm^{-2})	0.340	0.374	0.633	1.02

The CVs of nm-Pt/GC(n) electrodes are almost the same shape and in a good agreement with the bulk-Pt electrode except for slight the shift of the band positions. Therefore, the electrochemical characterization can also confirm that the nm-Pt/GC(n) electrodes are in the same surface morphology with the increase of the aggregation degree of Pt NPs. The bulk-Pt electrode surface could be considered as completely covered with a layer of Pt NPs, which has the highest aggregation degree.

2. Supplementary BB-SFG spectra

Figure S3 displayed the normalized BB-SFG spectra of that shown in Figure 1, a better comparison of line shapes could be obtained. It is clear that the linewidth changes dramatically with the structural change.

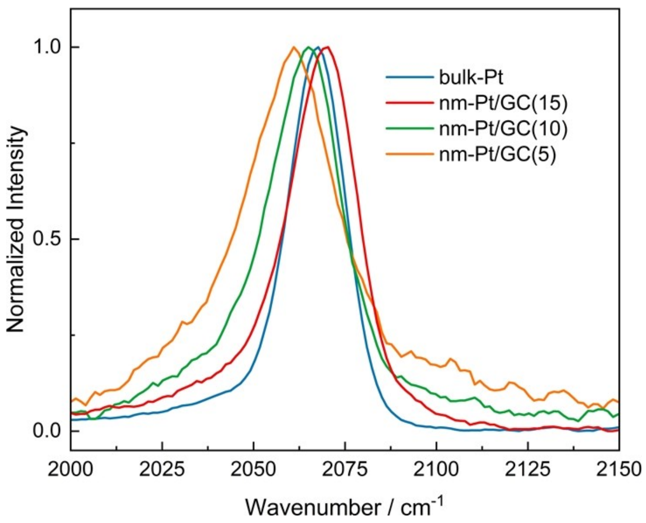

Figure S3. Normalized BB-SFG spectra of CO adsorbed on bulk-Pt and nm-Pt/GC electrodes in 0.1 M H_2SO_4 solution at 0.0 V.

We tried to reproduce the experimental spectra using a single peak with Lorentzian, Gaussian, or Voigt line shape models. For nm-Pt/GC(5), a single Lorentzian is capable of fitting the measured BB-SFG spectrum very well. But there are significant residuals for the fittings using any single peak model for the spectra of other electrodes, as shown in Figure S4. For the line shape on nm-Pt/GC(5), a single Lorentzian could reproduce the spectrum very well, which corresponding to the resonant SFG response from the linearly bonded CO (CO_L) on Pt. By adding the NR part to the fitting model (using Equation S2, the red curves in Figure S5), we found that the fitting quality is not significantly improved, but with higher uncertainties on the major fitting parameters. Especially for nm-Pt/GC(15) and bulk-Pt, obvious mismatches on both sides can be clearly seen (with significant residuals), as shown in Figure S5 (c) and (d). Thus, we believe that the NR contributions cannot be account for the non-symmetry line shape. As single peak could not fit all the spectra in Figure 1, we introduce the two-peak model as noted in the main text. This simplified two-resonance model could fit the measured BB-SFG spectral on all electrodes and those with different surface potentials. The fitting parameters are summarized in Table S2. The area ratio between the Gaussian and Lorentzian peaks varies from 0 to 3.0 with the aggregation of Pt NPs, which implies the structural effect on the inhomogeneity of CO_L.

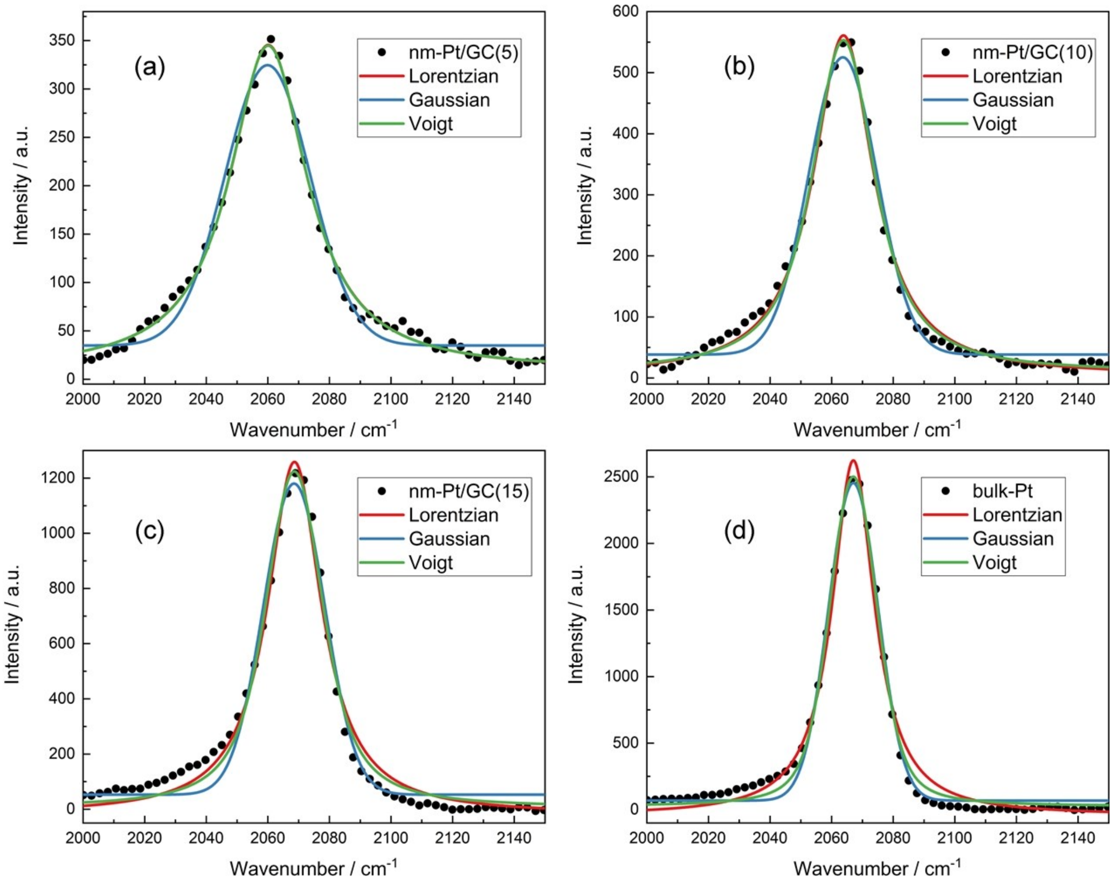

Figure S4. Comparison of single peak fitting using different line shapes (red for Lorentzian, blue for Gaussian, and green for Voigt) of the BB-SFG spectra of CO on (a) nm-Pt/GC(5), (b) nm-Pt/GC(10), (c) nm-Pt/GC(15), and (d) bulk-Pt electrode in 0.1M H_2SO_4 solution at 0.0 V.

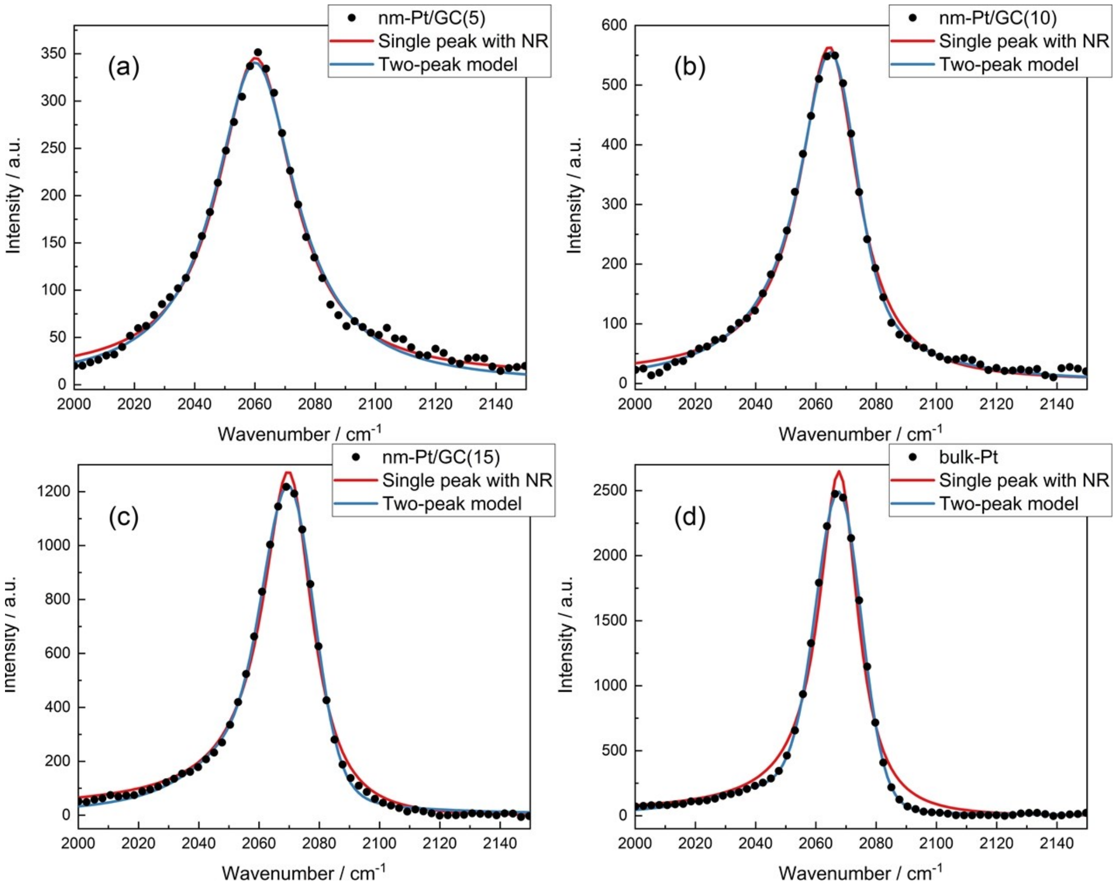

Figure S5. The comparison of fitting results using single-peak with NR (Equation S2) and two-peak model for the BB-SFG spectra of CO on (a) nm-Pt/GC(5), (b) nm-Pt/GC(10), (c) nm-Pt/GC(15), and (d) bulk-Pt electrode in 0.1M H_2SO_4 solution at 0.0 V.

Table S2. Parameters derived from spectral fittings with the two-peak model.

	Area_L / a.u.	ω_L / cm^{-1}	FWHM_L / cm^{-1}	Area_G / a.u.	ω_G / cm^{-1}	FWHM_G / cm^{-1}
nm-Pt/GC(5)	15081	2060 ± 0.1	32.8 ± 0.8	/	/	/
nm-Pt/GC(10)	13842	2059 ± 0.5	36.5 ± 1.2	891	2067 ± 0.5	14.3 ± 0.7
nm-Pt/GC(15)	15289	2053 ±1.2	40.0 ± 1.6	8236	2071 ± 0.3	16.1 ± 0.3
bulk-Pt	11049	2040 ± 1.5	42.9 ± 2.6	30172	2068 ± 0.2	16.4 ± 0.3

	A_L / a.u.	ω_L / cm^{-1}	Γ_L / cm^{-1}	θ / rad	A_G / a.u.	ω_G / cm^{-1}	$\Delta\omega_G$ / cm^{-1}
nm-Pt/GC(5)	302.3	2060 ± 0.1	16.4 ± 0.4	/	/	/	/
nm-Pt/GC(10)	308.4	2059 ± 0.5	18.2 ± 0.6	4.5	7.6	2067 ± 0.5	8.6 ± 0.4
nm-Pt/GC(15)	323.9	2053 ±1.2	19.9 ± 0.8	4.2	23.0	2071 ± 0.3	10.1 ± 0.2
bulk-Pt	309.3	2040 ± 1.5	21.4 ± 1.3	4.2	41.6	2068 ± 0.2	9.8 ± 0.2

There are many factors that could affect the SFG intensities for nanostructured electrodes, such as the surface structures, reflection and scattering properties. Actually, we got the relative interfacial CO oscillator densities by integrating the peak areas on every electrode and taking the reflectance and electrochemistry surface sites diversities into consideration. Similar to AIREs, the intensity of CO band was enhanced on the nanostructured electrodes, the enhancement factors are around 6, as shown in Table S3. However, this is a rough estimate and we did not observe the SFG enhancement in the raw spectra (due to scattering from the surface roughness). We could not make definite conclusion about the SFG enhancement. In the main text, we focused on the line shape and relative magnitude of the two peaks on different electrodes.

Table S3. SFG enhancement factor *A* of Pt/GC system calculated by considering different structural and optical corrections.

	bulk-Pt	nm-Pt/GC(5)	nm-Pt/GC(10)	nm-Pt/GC(15)
Peak Area	63379.13	18064.09	22267.03	38005.01
ECSA / cm^{-2}	0.340	0.374	0.633	1.02
SFG Reflectivity	1	0.26	0.27	0.31
VIS Reflectivity	1	0.23	0.26	0.30
IR Reflectivity	1	0.41	0.44	0.45
A	/	10.6	6.1	4.8

The corresponding potential-dependent BB-SFG spectra discussed in Figure 4 are shown in Figure S6 (at zero-time delay, the VIS and IR pulses reach the surface at the same time). The potential-dependent FWHM and area are displayed in Figure S7.

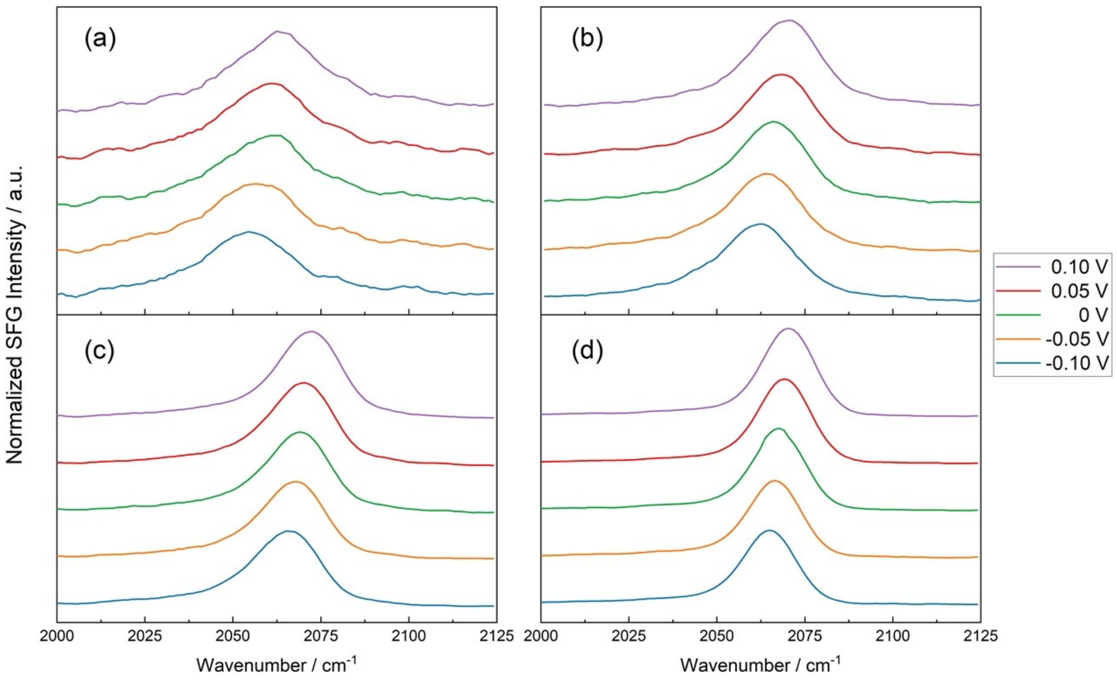

Figure S6. Potential-dependent BB-SFG spectra of CO adsorbed on (a) nm-Pt/GC(5), (b) nm-Pt/GC(10), (c) nm-Pt/GC(15) and (d) bulk-Pt electrode in 0.1M H_2SO_4 solution. Offset for comparison.

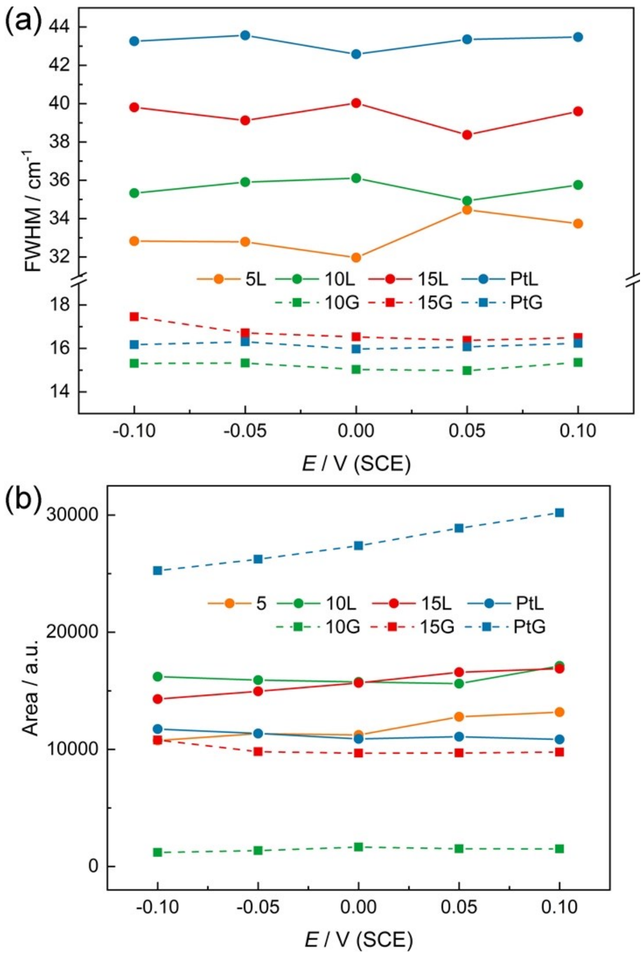

Figure S7. Potential-dependent (a) FWHM and (b) area for the Lorentzian (L) and Gaussian (G) peaks. (5, 10 and 15 denote the three nm-Pt/GC electrodes, Pt for bulk-Pt electrode.)

3. PCGP algorithm

Details of the principle component generalized projections (PCGP) algorithm was discussed previously.[2, 14, 15]

In BB-SFG, as only the IR is in resonant with the sample, the SFG signal at delay time τ can be expressed as

$$I_{SFG}(\omega_{SFG},\tau) = \left|\left(\chi^{(1)}(\omega_{IR})E_{IR}(\omega_{IR})\right)\otimes E_{VIS}(\omega_{VIS},\tau)\right|^2$$

$$= \left|P^{(1)}(\omega_{IR})\otimes\left(E_{VIS}(\omega_{VIS},0)e^{-i\omega_{VIS}\tau}\right)\right|^2 \quad \text{Equation S4}$$

$P^{(1)}$ is the IR-induced first-order polarization, which contains vibrational intensity, phase, line shape and other important information. By analyzing the SFG intensity in the frequency domain, $I_{SFG}(\omega_{SFG},\tau)$, with PCGP, we can reconstruct $P^{(1)}$ and E_{VIS}. Herein, the time-resolved BB-SFG spectra used for PCGP analysis were taken between τ = -3.8 ~ 3.8 ps with 0.21 ps interval (37 spectra). The interpolated BB-SFG spectrum at each delay time is from ω_{SFG} = 1875 to 2275 cm^{-1} with $\Delta\omega$ = 1 cm^{-1}. The simulation range for $P^{(1)}$ and E_{SFG} are from 1950 to 2200 cm^{-1}. The ERRORs converge to 10% within 600 iterations (<3 min computing time). Figure S8 presents the measured (circles) and PCGP reconstructed (lines) BB-SFG spectra.

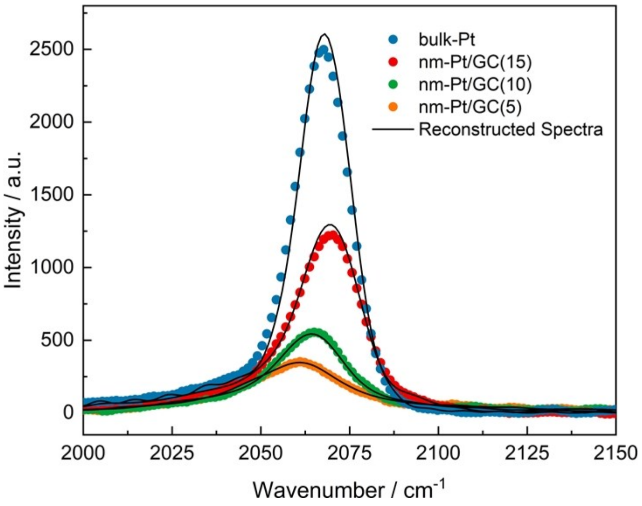

Figure S8. Measured (circles) and PCGP reconstructed (lines) BB-SFG spectra for CO on different nm-Pt/GC electrodes.

From PCGP, we can obtain decay properties of the vibrational resonance in the time domain without the interference of the input laser pulse and line shapes. The corresponding dynamic data in the time domain are summarized in Figure 2. The dephasing process (with both the pure dephasing and other inhomogeneous broadenings) is strongly associated with the molecular environments. The reconstructed SFG intensity in the time domain, Figure 2, also indicated that there were two kinds of CO_L in different chemical environments which dephasing with distinct time constants. The main part of the data on each electrode matches with a linear fit. We compared the dephasing time (T_2) and corresponding FWHM calculated from Figure 2 with that from the spectral analysis of Figure 1. Results are shown in Table S4. As the aggregation of the Pt NPs, the data points at short delay times started to off the linear fitting, especially of the bulk-Pt, data points before 0.4 ps are totally off the linear fitting line. Table S4 displays the dephasing time (T_2) and the corresponding peak width (FWHM = $1/(\pi c T_2)$) from Figure 2, and the spectral band width from the measured spectra in the right column. The time resolved result matches with the spectrum very well for the Pt/GC(5) electrode, and off-match with increase of Pt NPs aggregation. These properties suggest that there is more than one process involved in the dephasing dynamics. The linear part in Figure 2 for high aggregated Pt electrodes could not represent the whole character of CO_L. Thus, we proposed a simplified two-peak model to describe CO_L in two chemically different environments. The Lorentzian-like and Gaussian-like (Lorentzian and Gaussian in the main text) SFG peaks are corresponding to two types of CO_L which exhibited different frequencies and dephasing times. The Lorentzian-like component was originated from the relatively free distribution on island structured Pt. This form is dominant on nm-Pt/GC(5), resulting in the nearly Lorentzian line shape. As the aggregation of the Pt nanoparticles, we observed the increase of the Gaussian-like component, which was the feature of forced or compressed states (stronger interactions between surface species).

Table S4. Dephasing time constant T_2 and spectral width (FWHM) of CO_L.

	Time domain analysis		Spectral analysis
	T_2 / s	FWHM / cm^{-1}	FWHM / cm^{-1}
nm-Pt/GC(5)	0.344	30.8	30.9
nm-Pt/GC(10)	0.453	23.4	24.4
nm-Pt/GC(15)	0.601	17.6	22.5
bulk-Pt	0.746	14.2	18.7

4. *In situ* FTIRS

Figure S9 displays the FTIR spectra of these electrodes with one monolayer CO_{ad} at $E_S = 0.0$ V. One band between 2050 and 2100 cm^{-1} is assigned to the linearly bonded CO (CO_L). The positive-going band around 2343 cm^{-1} is attributed to the IR absorption of solution CO_2 species from CO_{ad} oxidation at the reference potential. As CO_{ad} only exists at E_S and the oxidation product CO_2 was exactly the opposite, the IR band directions of the two species should be negative and positive going, respectively. For the three nm-Pt electrodes, the direction of CO_L band is inverted, in addition, line shapes and intensity variations are also abnormal for these electrodes, which are consistent with the AIREs previously reported by Sun *et al.*[16-20]

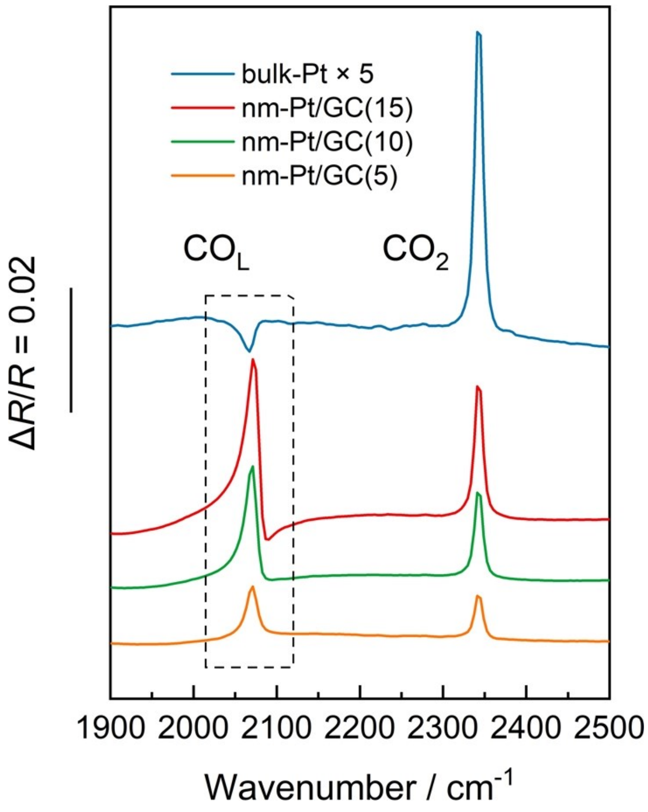

Figure S9. *In situ* FTIR spectra of CO adsorbed on bulk-Pt and nm-Pt/GC electrodes in 0.1 M H_2SO_4 solution, $E_S = 0.0$ V, $E_R = 0.8$ V.

The intensity of CO_2 IR band could be used to measure the quantity of CO_{ad}. We firstly measure the surface roughness (R) of the nm-Pt/GC electrodes for CO adsorption,

$$R_{\mathrm{Pt/GC}}^{\mathrm{CO_L}} = \frac{A_{\mathrm{Pt/GC}}^{\mathrm{CO_2}}/S_{\mathrm{Pt/GC}}}{A_{\mathrm{Pt}}^{\mathrm{CO_2}}/S_{\mathrm{Pt}}} \qquad \text{Equation S5}$$

where $S_{\mathrm{Pt/GC}}$ and S_{Pt} are the geometric surface areas of the nm-Pt/GC and the Pt electrodes, $A_{\mathrm{Pt/GC}}^{\mathrm{CO_2}}$ and $A_{\mathrm{Pt}}^{\mathrm{CO_2}}$ are the integrated intensities of the CO_2 IR band of the spectra for the two kinds of electrodes respectively. Then, the IR enhancement factor $\Delta_{\mathrm{Pt/GC}}^{\mathrm{CO_L}}$ could be calculated,

$$\Delta_{\mathrm{Pt/GC}}^{\mathrm{CO_L}} = \frac{R_{\mathrm{Pt/GC}}^{\mathrm{CO_L}}}{R_{\mathrm{Pt}}^{\mathrm{CO_L}}} = \frac{1}{R_{\mathrm{Pt}}^{\mathrm{CO_L}}} \frac{A_{\mathrm{Pt/GC}}^{\mathrm{CO_L}}/S_{\mathrm{Pt/GC}}}{A_{\mathrm{Pt}}^{\mathrm{CO_L}}/S_{\mathrm{Pt}}} \qquad \text{Equation S6}$$

where $A_{\mathrm{Pt/GC}}^{\mathrm{CO_L}}$ and $A_{\mathrm{Pt}}^{\mathrm{CO_L}}$ are the integrated intensities of the $\mathrm{CO_{ad}}$ IR band for nm-Pt/GC and the Pt electrodes respectively.[16] The values of $\Delta_{\mathrm{Pt/GC}}^{\mathrm{CO_L}}$ calculated from Figure S9 and display in Table S5. The value of $\Delta_{\mathrm{Pt/GC}}^{\mathrm{CO_L}}$ is around 10, which demonstrates that the IR absorption of $\mathrm{CO_{ad}}$ on nm-Pt/GC electrodes were enhanced. Noticing that, the SFG enhancement factor in Table S3 is about the same order of magnitude, indicating that the reasons of enhancements in IR and SFG might be similar.

Table S5. IR enhancement factor $\Delta_{\mathrm{Pt/GC}}^{\mathrm{CO_L}}$ and related parameters for Pt/GC systems.

	Pt	nm-Pt/GC(5)	nm-Pt/GC(10)	nm-Pt/GC(15)
$A^{\mathrm{CO_2}}$	0.1488	0.0963	0.2072	0.3118
A^{CO}	0.0220	0.1721	0.3644	0.6623
$R_{\mathrm{Pt/GC}}^{\mathrm{CO_L}}$	1	0.5883	0.7479	0.6984
$\Delta_{\mathrm{Pt/GC}}^{\mathrm{CO_L}}$	1	12.09	11.90	13.42

Compared the SFG spectra in Figure 1 in the main text and FTIR spectra in Figure S9, we could see the comparison between the two spectroscopies. As shown in Figure S10, the FTIR spectrum of $\mathrm{CO_{ad}}$ on Polycrystalline Pt has the same asymmetric feature and the trailing is at low frequency side. Turn to nano structure electrodes, the changes of line shapes are not significant as FTIR results, where for nm-Pt/GC(5) is anti-absorption AIREs, for nm-Pt/GC(15) is a Fano-like line shape and a transition line shape for nm-Pt/GC(10).

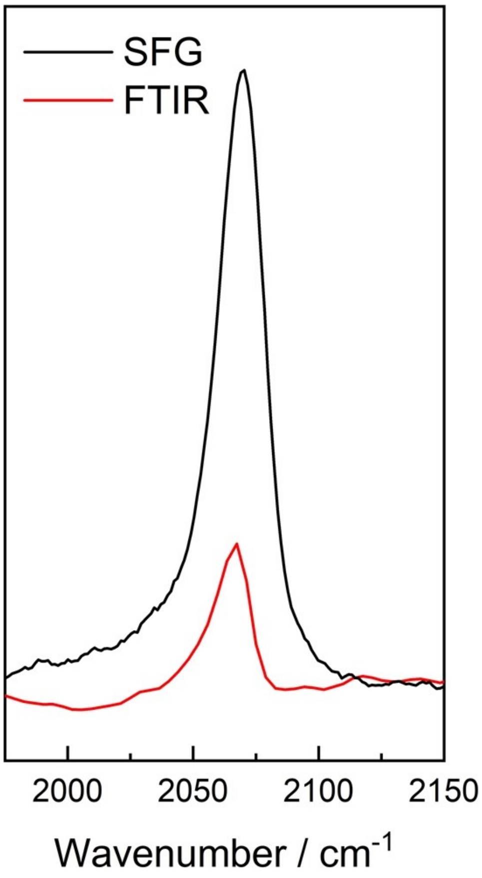

Figure S10. Comparison of SFG and FTIR spectra for CO adsorbed at Pt electrode (scale and peak direction adjusted by mathematical processing).

The potential dependent FTIR spectra were collected using multistep FTIR spectroscopy (MSFTIRS) procedures. MSFTIRS spectra of CO adsorption on each Pt electrode are displayed in Figure S11. There are no intensity changes of both CO_L and CO_2 IR bands before the onset of CO oxidation (~ 0.2 - 0.2 V), which indicates that CO remained stable adsorption on Pt before oxidation. The increase of peak area for two SFG peaks in Figure S7 b as potential stepped from -0.1 V to 0.1 V might possibly be related to the changes in surface orientation and hyperpolarizability of CO_L. The Stark effect of the CO_{ad} obtained on these Pt electrodes (before the onset potential of CO oxidation/pre-oxidation) is around 27 $cm^{-1} \cdot V^{-1}$, which is similar to the corresponding Stark slope of the Lorentzian BB-SFG peak. The relationship between AIREs and line shape variations in BB-SFG spectra need further analysis, and will be discussed in our future publication.

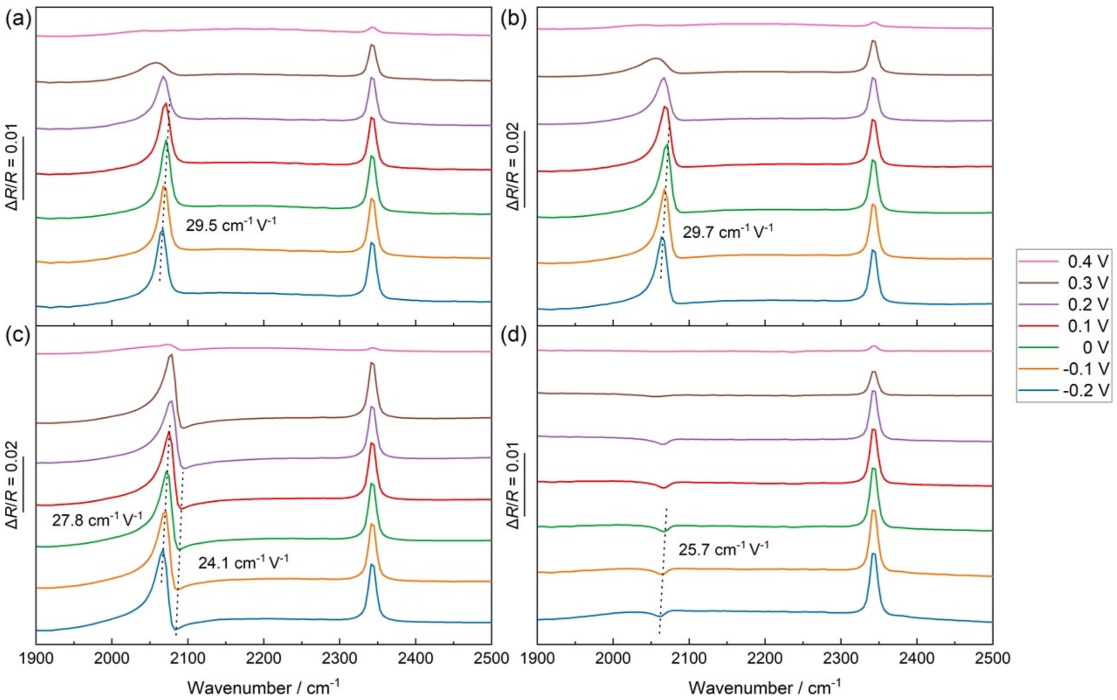

Figure S11. Potential-dependent MSFTIRS spectra of CO adsorbed on (a) nm-Pt/GC(5), (b) nm-Pt/GC(10), (c) nm-Pt/GC(15) and (d) bulk-Pt electrode in 0.1M H_2SO_4 solution, E_R = 0.8 V. Offset for comparison.

5. Illustration of surface adsorption of CO_L

For nm-Pt/GC(5), the electrode with the lowest aggregation degree of Pt nanoparticles, the spectrum is very close to a Lorentzian line shape, which indicates adsorbed CO distribution is homogeneous for island structured Pt. As the aggregation of the Pt nanoparticles, we observed the increase of the Gaussian-like component. The corresponding inhomogeneity is originated from the adsorbed CO distribution over the entire Pt surface sites, which is related to the effect of Pt nanoparticles aggregation. If we model the Pt NPs as a perfect sphere, and all the surface CO can be perpendicular to the surface on an isolated Pt NP. This is a “homogeneous” adsorption with less interactions between the surface COs. On a flat surface, there will be stronger interactions between the COs, and there will be not enough room spatially for all the COs to be perfectly perpendicular to the surface, thus there is more “inhomogeneity” in the surface orientations with respect to the Pt surface. In the sense of packing, it is relatively closer or more ordered packing on a flat surface. We think the exact surface states of adsorbed CO are too complicated and hard to characterize accurately, there are too many possibilities. We inferred the possible corresponding states of Lorentzian and Gaussian from the relative values of peak position, width and Stark slope. A narrower width and a higher frequency indicate the forced and compressed states, which was similar to the compressed CO on Pd observed by Ouvrard *et al.* We believe that the results here would be helpful for the understanding of the adsorption of CO on nanostructured Pt surfaces.

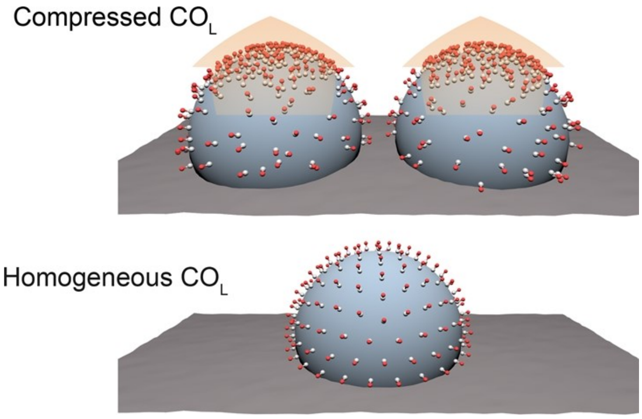

Figure S12. Illustrated surface adsorption configuration of CO_L. The homogeneous CO_L (bottom) corresponding to the Lorentzian peak, and the relatively compressed CO_L on Pt NPs (top) corresponding to the Gaussian peak.

References

1. Q. Cen, Y. He, M. Xu, J. Wang and Z. Wang, *J Chem Phys*, 2015, **142**, 114201.
2. Y. He, Y. Wang, J. Wang, W. Guo and Z. Wang, *Opt. Lett.*, 2016, **41**, 874-877.
3. J. J. Wang, M. Xu, Z. C. Huangfu, Y. Wang, Y. H. He, W. Guo and Z. H. Wang, *Vibrational Spectroscopy*, 2016, **85**, 122-127.
4. Z. C. Huang-Fu, Q. T. Song, Y. H. He, J. J. Wang, J. Y. Ye, Z. Y. Zhou, S. G. Sun and Z. H. Wang, *Phys Chem Chem Phys*, 2019, **21**, 25047-25053.
5. C. L. A, M. S. T and W. W. E, *Journal*, 1975.
6. X. D. Zhu, H. Suhr and Y. R. Shen, *Phys Rev B Condens Matter*, 1987, **35**, 3047-3050.
7. Y. R. Shen, *Nature*, 1989, **337**, 519-525.
8. Y. R. Shen, *Annual Review of Physical Chemistry*, 1989, **40**, 327-350.
9. Y. R. Shen, *Applied Physics a-Materials Science & Processing*, 1994, **59**, 541-543.
10. Y. R. Shen, *Surface Science*, 1994, **299**, 551-562.
11. Y. R. Shen, *The Journal of Physical Chemistry C*, 2012, **116**, 15505-15509.
12. S.-G. Sun and Y. Lin, *Electrochimica Acta*, 1998, **44**, 1153-1162.

13. J.-Y. Ye, Y.-X. Jiang, T. Sheng and S.-G. Sun, *Nano Energy*, 2016, **29**, 414-427.
14. D. J. Kane, *J. Opt. Soc. Am. B*, 2008, **25**, A120-A132.
15. Y. He, Y. Zhang, H. Ren, J. Wang, W. Guo, S.-G. Sun and Z. Wang, *Opt. Express*, 2019, **27**, 28564-28574.
16. G.-Q. Lu, S.-G. Sun, S.-P. Chen and L.-R. Cai, *Journal of Electroanalytical Chemistry*, 1997, **421**, 19-23.
17. G.-Q. Lu, S.-G. Sun, L.-R. Cai, S.-P. Chen, Z.-W. Tian and K.-K. Shiu, *Langmuir*, 2000, **16**, 778-786.
18. W.-G. Lin, S.-G. Sun, Z.-Y. Zhou, S.-P. Chen and H.-C. Wang, *The Journal of Physical Chemistry B*, 2002, **106**, 11778-11783.
19. H. C. Wang, S. G. Sun, J. W. Yan, H. Z. Yang and Z. Y. Zhou, *J Phys Chem B*, 2005, **109**, 4309-4316.
20. Q.-S. Chen, S.-G. Sun, J.-W. Yan, J.-T. Li and Z.-Y. Zhou, *Langmuir*, 2006, **22**, 10575-10583.